Supplementary Figure S1

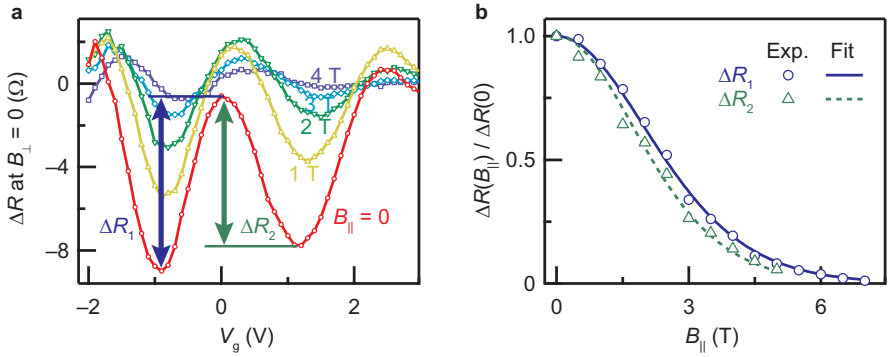

Supplementary Figure S1: **Suppression of quantum interference due to spin-dependent time-reversal symmetry breaking. (a)** Altshuler-Aronov-Spivak amplitude at zero perpendicular magnetic field ($B_\perp = 0$) as a function of the gate voltage V_g [corresponding to the Aharonov-Casher (AC) effect] at a number of different in-plane $B_\parallel$-fields. Arrows indicate the amplitudes of the AC oscillations. **(b)** Suppression of the AC amplitude by $B_\parallel$. Vertical axis represents the normalized AC amplitude, i.e., the AC amplitude $\Delta R(B_\parallel)$ divided by the AC amplitude at $B_\parallel = 0$, $\Delta R(0)$. Lines are the fit to the experimental data using equation (S3), with c being treated as a fitting parameter.

Supplementary Figure S2

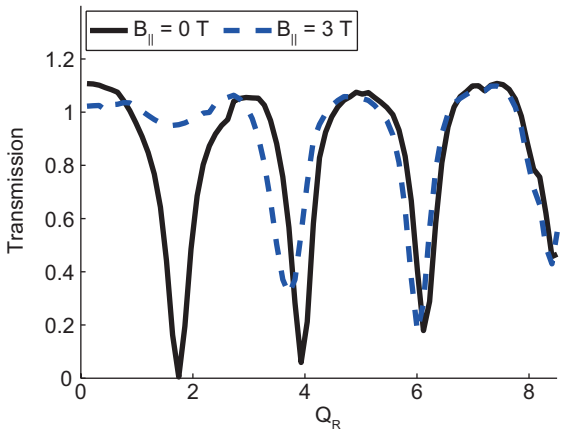

Supplementary Figure S2: **Aharonov-Casher conductance oscillations in a quasi-1D ballistic quantum ring as calculated by the recursive Green's function method.** The conductance is plotted as a function of scaled spin-orbit field Q_{R}. An in-plane magnetic field $B_{||}$ induces an interference dip shift as shown by the dashed line. The ring diameter $r = 608\,\mathrm{nm}$ and g-factor is 3. The ring aspect ratio low $W/r = 0.025$. Transmission is averaged between energies 48 meV and 49 meV.

Supplementary Figure S3

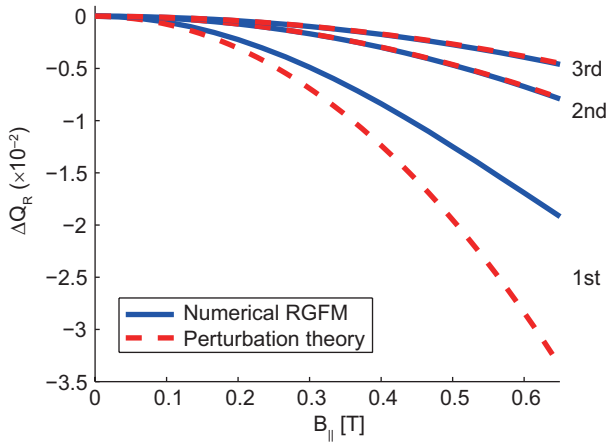

Supplementary Figure S3: **Aharonov-Casher interference dip shift as a function of external in-plane magnetic field $B_{\parallel}$ in a quasi-1D (single-mode) ballistic quantum ring.** Dip shifts are shown for the first three dips. The solid lines show recursive Green's function calculations and the dashed lines show perturbation calculation in the low magnetic field limit. The ring aspect ratio is $W/r = 0.025$. The ring diameter $r = 608\,\mathrm{nm}$ and g-factor is 3. Transmission is averaged between energies 48 meV and 49 meV.

Supplementary Figure S4

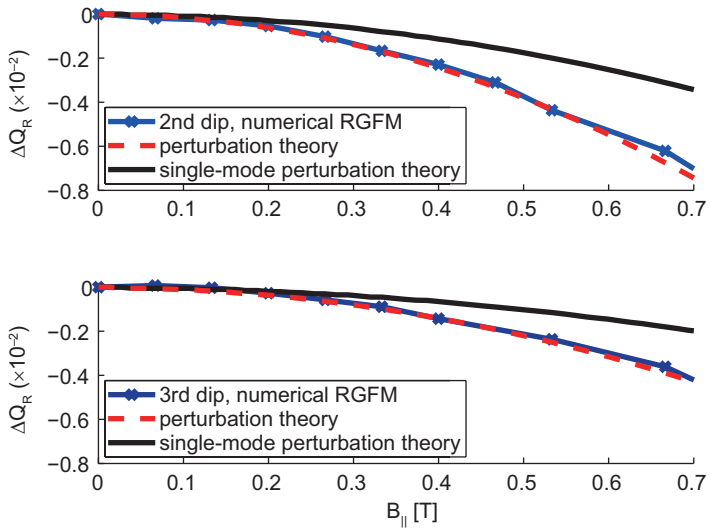

Supplementary Figure S4: **Dip shifts for the second and third Aharonov-Casher interference dips in a ballistic quantum ring with 6 transport modes (upper and lower panels, respectively).** Low field dip shifts are accurately described by the perturbation theory assuming independent mode transport. The dip shift is larger than for quasi-1D system with k determined from the 2DEG carrier density (black solid line). The ring diameter $r = 608\,\mathrm{nm}$, g-factor is 3 and the wire is 75 nm wide. Transmission is averaged between energies 48 meV and 49 meV.

Supplementary Figure S5

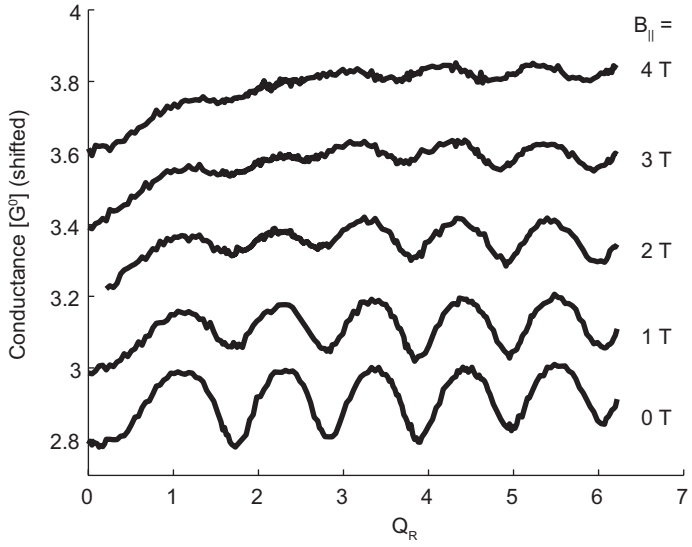

Supplementary Figure S5: **Aharonov-Casher effect in a disordered multi-mode ring at different in-plane magnetic fields $B_{\parallel}$.** The figure shows Altshuler-Aronov-Spivak conductance oscillations as a function of scaled spin-orbit field strength Q_{R}. The ring diameter $r = 608\,\mathrm{nm}$, g-factor is 4, $m^{\star} = 0.05\,m_0$ and mean free path is $2\,\mu$m. The conducting wire is 75 nm wide and transmission is averaged between energies 48 meV and 48.5 meV. The number of transport modes per spin is 6. Curves for $B_{\parallel} > 0$ have been shifted for clarity.

Supplementary Figure S6

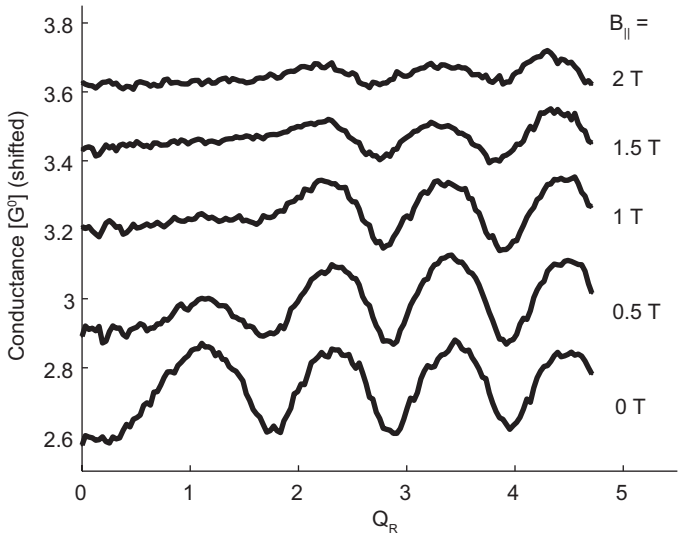

Supplementary Figure S6: **Averaged conductance through ballistic multi-mode rings with lead displacement $\Delta y = \pm 24\,\mathrm{nm}$ at different in-plane magnetic fields $B_{\parallel}$.** Conductance shows Altshuler-Aronov-Spivak oscillations as a function of scaled spin-orbit field strength Q_{R}. The ring diameter is $r = 608\,\mathrm{nm}$, $m^{\star} = 0.05\,m_0$ and g-factor is 4. The conducting wire is 75 nm wide. Transmission is averaged between energies 48 meV and 48.5 meV supporting 6 transport modes per spin. Curves for $B_{\parallel} > 0$ have been shifted for clarity.

Supplementary Note 1. SUPPRESSION OF SPIN INTERFERENCE BY AN IN-PLANE MAGNETIC FIELD

In a system with time-reversal (TR) symmetry, competition between Rashba spin-orbit (SO) interaction and Zeeman coupling of the in-plane magnetic field $B_{\parallel}$ induces spin-dependent dephasing as a result of TR symmetry breaking. These couplings do not solely break TR symmetry, but their competition affects the phase coherence through a dynamical phase of electron spins, i.e., a phase accumulated by the spin precession. Previously, interplay of Rashba SO interaction and in-plane Zeeman coupling has been studied in an InGaAs two-dimensional electron gas (2DEG) [26, 33]. The $B_{\parallel}$-field dependence of the phase-coherence time $\tau_{\varphi}(B_{\parallel})$ for TR interference in a 2DEG has been theoretically predicted as the following equation [34]:

$$\frac{\tau_{\varphi}(B_{\parallel})}{\tau_{\varphi}(0)} = \frac{1}{1+cB_{\parallel}^2}\,, \tag{S1}$$

where c is a constant denoted by $c = \tau_{\varphi}(0)\tau_{\rm SO}(0)(g^{\star}\mu_{\rm B}/\hbar)^2$, with $\tau_{\rm SO}(B_{\parallel})$ being the SO relaxation time at $B_{\parallel}$. Further, $g^{\star}$ is the Landé g-factor and $\mu_{\rm B}$ is the Bohr magneton. We apply the theory to TR interference in a ring structure as a following way. We assume that the Altshuler-Aronov-Spivak amplitude at $B_{\parallel}$, $\Delta R(B_{\parallel})$, is reduced by the factor of $\exp\left[-4\pi r/l_{\varphi}(B_{\parallel})\right]$, where r is the radius of a ring and $l_{\varphi}(B_{\parallel})$ is the phase-coherence length at $B_{\parallel}$. Here, by using equation (S1), $l_{\varphi}(B_{\parallel})$ is given by

$$l_{\varphi}(B_{\parallel}) = \sqrt{D\tau_{\varphi}(B_{\parallel})} = l_{\varphi}(0)\sqrt{\frac{1}{1+cB_{\parallel}^2}}\,, \tag{S2}$$

where D is the diffusion constant. The spin-dependent dephasing rate can be probed by the following equation:

$$\frac{\Delta R(B_{\parallel})}{\Delta R(0)} = \exp\left[-4\pi r\left(\frac{1}{l_{\varphi}(B_{\parallel})} - \frac{1}{l_{\varphi}(0)}\right)\right]. \tag{S3}$$

As shown in Supplementary Fig. S1a, the experimentally obtained Aharonov-Casher (AC) oscillations are suppressed by applying $B_{\parallel}$. We define the resistance amplitudes ΔR_1 and ΔR_2 as the arrows shown in Supplementary Fig. S1a. The $B_{\parallel}$ dependence of these amplitudes is shown in Supplementary Fig. S1b. The open symbols are the experimental results and the lines are fits to the experimental data using equation (S3), where we treat c as a fitting parameter. We note that the phase-coherence time $\tau_{\varphi}(0)$ can be obtained from the amplitude of the Altshuler-Aronov-Spivak oscillations at $B_{\parallel} = 0$ [35]. From the fit to the data, we have obtained $\tau_{\rm SO}(0) \sim 0.2\,$ps for the $\Delta R_1(B_{\parallel})/\Delta R_1(0)$ curve and $\tau_{\rm SO}(0) \sim 0.4\,$ps for the $\Delta R_2(B_{\parallel})/\Delta R_2(0)$

curve. These values are reasonable for our measured Rashba SO coupling constants. Thus, the suppression of AC interference by $B_{\|}$ is explained in terms of the spin-dependent dephasing caused by competition between Rashba SO coupling and Zeeman coupling. In conclusion, the influence of the in-plane $B_{\|}$-field on AC interference has two components: suppression of the AC amplitude through the dynamical phase and a geometric-phase shift of the AC phase as shown in the main text.

Supplementary Note 2. NUMERICAL TRANSPORT CALCULATIONS

Overview

The perturbation theory results apply for a single channel quantum ring in a weak Zeeman field and in the absence of disorder. However, in the experiments the conductive channels in the ring array support multiple transport modes. In the perturbation theory the geometric phase shift is proportional to $1/k^2$, where k is the wave vector parallel to the ring. Therefore the phase shift depends on the transport mode. Moreover, the spin-orbit field strength at the first interference peak positions is comparable to the Zeeman field strength. The in-plane magnetic field also causes significant dephasing as shown by the decreasing oscillation amplitude in experiments. In order to gain more understanding of phase shifting and dephasing we applied multi-mode spin-dependent quantum transport calculations using a numerical recursive Green's function (RGF) algorithm.

The system in the calculations consists of a ring which is connected to two leads. We work within the framework of the Landauer-Büttiker formalism [36, 37] and take Hamiltonian

$$H = \frac{1}{2m^\star}\mathbf{P}^2 + \frac{\alpha_\mathrm{R}}{\hbar}(P_x\sigma_y - P_y\sigma_x) + \frac{1}{2}g^\star\mu_\mathrm{B}B_\parallel\sigma_x + V_\mathrm{dis}(\mathbf{x}), \tag{S4}$$

as the starting point. Here, $\mathbf{P}$ is the kinetic momentum, $m^\star$ the electron's effective mass, α_R the strength of Rashba spin-orbit coupling, σ_i the Pauli matrix in the i direction, $g^\star$ the Landé g-factor, μ_B the Bohr magneton, $B_\parallel$ the in-plane magnetic field and $V_\mathrm{dis}(\mathbf{x})$ the disorder potential at the position $\mathbf{x}$. Transmission is calculated using the RGF algorithm which is based on a tight-binding discretization of the 2D system using square grid elements [28]. The grid spacing in calculations vary between 1 nm and 3 nm. The transmission coefficients from mode n to m, t_{nm}, are calculated within the RGF algorithm and conductance G is then obtained from the Landauer formula

$$G(B_\parallel) = \frac{e^2}{h}\sum_{n,m,\sigma,\sigma'}\left|t^{\sigma\sigma'}_{nm}(B_\parallel)\right|^2, \tag{S5}$$

where σ denotes the spin index. The spin-orbit coupling and the Zeeman coupling of the in-plane field are turned on and off adiabatically in the leads. The contacts to the ring are slightly rounded. The width of the conducting wire in the simulations is of the order of 50 nm. We assume in the calculations that the wire has square well confining potential perpendicular to the transport direction and therefore supports 4 to 6 transport modes at the carrier densities measured in InGaAs 2DEG. Conductances are given in units

of $G^0 = e^2/h$ unless stated otherwise.

We use an Anderson-like disorder model to account for spin-independent scattering processes in the ring [38]. In experiments the ring array consists of rings of slightly varying geometries. Numerical calculations simulate this by performing conductance average over large number of different rings where the lead position has been shifted by Δy with respect to the ring center. To account for the finite temperature in experiments we average conductance over an energy window which has a width of 0.5 to 1 meV. The imperfect coupling of the leads to the ring leads to strong resonances in electron transport through the ring at resonance energies determined by the electron dynamics. Such signatures of dynamical phases are averaged out by performing the above averaging over different energies, disorder configurations and ring geometries. Geometric phases are largely unaffected by such averaging. The resulting conductance then shows oscillations due to interference of geometric phases. We still expect that k-dependence of the geometric phase shift for different transport channels may lead to broadening of the interference dips.

Ballistic transport regime

The mean free path in our experiments is comparable to the ring circumference. Therefore we assume for the moment ballistic electron transport in the ring. In order to compare the perturbation theory and the numerical algorithm we performed calculations in a quasi-1D ring with a single transport channel. The interference paths shown in Fig. 6a in the main text contribute to the Aharonov-Casher conductance oscillations. Conductance oscillations are described analytically by

$$G = \frac{e^2}{h}\left\{1 + \cos\left[\pi\left(\sqrt{1+Q_{\mathrm{R}}^2} - 1\right)\right]\right\}, \tag{S6}$$

where the scaled spin-orbit strength $Q_{\mathrm{R}} = 2\alpha_{\mathrm{R}} m^\star r/\hbar^2$ [23]. This has a maximum at vanishing spin-orbit coupling $Q_{\mathrm{R}} = 0$.

Supplementary Fig. S2 shows Aharonov-Casher conductance oscillations in a quasi-1D ballistic ring as calculated by the RGF method. In comparison to equation (S6) the interference peaks are narrow due to several possible windings of electrons around the ring. Application of an in-plane magnetic field shifts the dips to lower spin-orbit fields and dampens conductance oscillations in the low spin-orbit fields. This is a sign of dephasing [33, 39]. The shifts of the interference dips calculated with the RGF method are compared to the perturbation theory results in Supplementary Fig. S3 in the low magnetic field limit. The peak shifts show parabolic dependence on the magnetic field strength. The correspondence is very good for

the higher order peaks where the Zeeman energy is low in comparison to the spin-orbit energy as required by the perturbation calculation. Larger deviations are seen for the first peak where the spin-orbit energy is low.

The perturbation calculation at low Zeeman energies shows that the phase shift of a transport mode is proportional to $1/k^2$ [see equation (4)]. We assume here that the quantum well in the wire has a square shape and therefore the confinement energy is proportional to the square of the transverse mode number. The quantum well energy is then relatively low for the first modes in a wire which can occupy several modes. The phase shifts for these modes are therefore comparable but the shifts increase with n. Assuming that the modes are transported independently the total conductance shows a broad minimum with a larger displacement of the dip position compared to the lowest mode alone. Supplementary Fig. S4 shows dip displacements for the 2nd and 3rd dips in the low magnetic field limit in a 6-mode ring as calculated by the RGF method and compared to the perturbation calculations. In this limit the perturbation theory is in good agreement with the RGF calculations assuming that the modes are independently transported through the ring.

Conductance oscillations in disordered rings

In disordered rings scattering reduces the contribution of the Aharonov-Casher interference paths (Fig. 6a in the main text). It is further reduced by averaging over different ring geometries. However, when the ring has many conducting channels interference can still take place for paths which go around the ring in opposite directions as shown in Fig. 6b in the main text. The effect is caused by coherent backscattering due to constructive interference between time-reversed paths [37] and it gives rise to Altshuler-Aronov-Spivak (AAS) conductance oscillations [40]. In contrast to the Aharonov-Casher case the conductance oscillations of the AAS interference paths have a minimum at zero spin-orbit coupling and double oscillation frequency as a function of spin-orbit interaction strength.

Supplementary Fig. S5 shows AAS conductance oscillations in a disordered multi-mode ring at different in-plane magnetic field strengths. Finite in-plane magnetic fields dampen the conductance oscillations. The dampening is strongest in the regime where the Zeeman energy is large in comparison to the spin-orbit interaction energy (upper left hand side of the plot) and it is associated with dephasing as discussed in the previous section. The conductance drop in the small spin-orbit fields may be due to the weak antilocalization effect since it persists at large magnetic fields but disappears gradually with increasing electron mean free path. The figure shows that interference dips shift to lower spin orbit fields as the

in-plane magnetic field is increased. This is a sign of a geometric phase shift.

In experiments the rings in the array have slightly different geometries set by the accuracy in the manufacturing process. We model this by displacing the ring with respect to the leads by a random distance Δy. This makes one of the ring branches slightly longer than the other. Geometry averaged conductance through a ballistic ring shows AAS oscillations and strong dephasing in the regime of low spin-orbit fields (see Supplementary Fig. S6).

For the AAS interference paths the phase shift in the perturbation calculation is twice the phase shift for the Aharonov-Casher interference paths [see equation (3) in the main text]. However, conductance oscillations would show the same dip shifts in the spin-orbit field strength because the AAS conductance oscillation frequency is doubled and leads to only half the shift in the spin-orbit field [phase shift φ in $G' = \cos(2\alpha_\mathrm{R} + \varphi)$ shifts the minimum of G' by $\Delta\alpha_\mathrm{R} = \varphi/2$].

Simulations of experiments

The measured geometric phase shifts depend on a number of parameters in the experiments due to the presence of multiple transport channels. We choose the RGF method to simulate the actual phase shifts measured in the samples. The carrier density in the sample changes with the gate voltage. Spin-orbit interaction and carrier density were measured to be related according to formula $\alpha_\mathrm{R}\,[\mathrm{peV\,m}] = -7.81 + 3.32\,n_s\,[10^{16}\,\mathrm{m}^{-2}]$. The Dresselhaus spin-orbit interaction is expected to be small in comparison to the Rashba spin-orbit interaction and therefore the Dresselhaus term is omitted in the numerical model. The lead displacement is a random variable ranging between $\Delta y = \pm 12\,\mathrm{nm}$.

In the peak and dip shift calculations conductance was first calculated around these extrema. Since the computational configuration consists of a single ring the carrier density was increased stepwise in order to avoid discontinuities in conductance due to opening of new transport channels. Typically a few thousand disorder configurations were used and a second order polynomial was fitted to the conductance. The peak and dip positions are then extracted from the polynomial. The dip shifts are generally calculated only up to magnetic fields of 5 to 6 T. When the Zeeman field is large compared to the spin-orbit field dephasing makes the signal weak and dip positions are difficult to extract with high accuracy. We find that, to computational accuracy, the resistance peak shifts for the highest order peaks are independent of the disorder strength for electron mean free paths between 2 μm and 6 μm.

In the regime of high Zeeman energy in comparison to the spin-orbit energy (first resistance dip) the calculations show linear dependence on the magnetic field. The perturbation expansion is not valid in this

regime. Simulations show a quadratic geometric phase shift as a function of the in-plane magnetic field for the higher order peaks and dips. The phase shift in the RGF calculations may be larger than the phase shift for the lowest mode calculated in the perturbation theory. This is caused by the combined phase shift of several transport modes, as discussed above in the context of ballistic systems. See e.g. the phase shift calculated for the peak at $V_\mathrm{g} \sim -2\,\mathrm{V}$ (P1) in the Fig. 4 in the main text.

We have so far assumed that the conducting channel is a square quantum well in the transverse direction with eigenenergy proportional to n^2. In such a confining potential several eigenmodes contribute to conductance oscillations, as discussed above. However, the confining potential may be slightly rounded at the bottom. In a harmonic quantum well the eigenenergies are proportional to n. This may lead to much smaller k for the higher modes and, as a consequence, weak spin-orbit coupling and dephasing of these modes in high magnetic fields. Therefore only a few modes or just the lowest one may contribute significantly to conductance oscillations. A single-mode perturbation theory would then give the phase shifts accurately in the strong spin-orbit coupling regime. Qualitatively this is consistent with the measured peak-shift data at high spin-orbit fields. Accurate estimation of the exact phase shift in the calculations would require careful modeling of the confining potential in the conductive channel. This, however, is beyond the scope of this work. We conclude that given the uncertainties in the modeled system properties and parameters the presented simulation results are in good agreement with the observed phase shifts.

Supplementary Note 3. EFFECT OF MODE MIXING

In the numerical calculations, we use Ando's lattice disorder model [38]. The (random) disorder potential can then be calculated from the formula (2.5) in Ando's paper:

$$\frac{W}{E_{\mathrm{F}}} = \sqrt{\frac{6\lambda_{\mathrm{F}}^3}{\pi^3 a^2 l_{\mathrm{MF}}}}, \tag{S7}$$

where λ_{F} is the Fermi wave length, a is the lattice spacing and l_{MF} is the mean free path. Using typical parameters in the calculations ($a = 3\,\mathrm{nm}$, $l_{\mathrm{MF}} = 2\,\mu\mathrm{m}$, $\lambda_{\mathrm{F}} = 25\,\mathrm{nm}$) we get $W/E_{\mathrm{F}} \simeq 0.4$. Therefore the disorder potential ranges from about -0.2 to 0.2 in units of the Fermi energy. Regarding the subband spacing, if we assume $E_{\mathrm{F}} \sim 60\,\mathrm{meV}$ and evenly spaced subband energy levels, the subband spacing is $10\,\mathrm{meV}$ (when the number of transverse modes ~ 6). Hence we expect mode mixing is significant in our system.

Usually, mode mixing does not harm the Altshuler-Aronov-Spivak (AAS) pattern as far as it is induced by elastic scattering (either from impurities or geometric asymmetries) and the rings aspect ratio remains small. Actually, from a semiclassical point of view, mode mixing helps to isolate the time-reversed paths leading to AAS oscillations from the rest (the contribution of which is averaged out). However, slow electrons propagating along higher modes may suffer from stronger decoherence. In this sense, mode mixing may reduce the AAS amplitude. The observed AAS oscillations are hence mainly due to scattering within the lowest modes (faster electrons).

Regarding the (geometric) phase shift, mode mixing leads to smearing of the shift, namely averaging of the quantity of the shift may occur. However, as we can see from a good agreement between experiment and the single-mode perturbation theory, the first lowest mode predominantly contributes to the geometric phase shift. That is why we did not experimentally observe smearing of the shift due to mode mixing. Note that in the above discussion we have considered the transverse modes, i.e., size-quantized modes in the radial direction of rings, and have not considered modes in the normal direction to the two-dimensional electron gas, since we only have a single mode in this direction.

Supplementary References

[33] Meijer, F. E., Morpurgo, A. F., Klapwijk, T. M. & Nitta, J. Universal spin-induced time reversal symmetry breaking in two-dimensional electron gases with Rashba spin-orbit interaction. *Phys. Rev. Lett.* **94,** 186805 (2005).

[34] Mal'shukov, A. G., Chao, K. A. & Willander, M. Magnetoresistance of a weakly disordered III-V semiconductor quantum well in a magnetic field parallel to interfaces. *Phys. Rev. B* **56,** 6436–6439 (1997).

[35] Umbach, C. P., Van Haesendonck, C., Laibowitz, R. B., Washburn, S. & Webb, R. A. Direct observation of ensemble averaging of the Aharonov-Bohm effect in normal-metal loops. *Phys. Rev. Lett.* **56,** 386–389 (1986).

[36] Landauer, R. Spatial variation of currents and fields due to localized scatterers in metallic conduction. *IBM J. Res. Develop.* **1,** 223–231 (1957).

[37] Büttiker, M., Imry, Y., Landauer, R. & Pinhas, S. Generalized many-channel conductance formula with application to small rings. *Phys. Rev. B* **31,** 6207–6215 (1985).

[38] Ando, T. Quantum point contacts in magnetic fields. *Phys. Rev. B* **44,** 8017–8027 (1991).

[39] Stern, A. & Entin-Wohlman, O. Damped conductivity oscillations resulting from the interplay of spin-orbit and Zeeman couplings. *Phys. Rev. B* **44,** 10976–10979 (1991).

[40] Al'tshuler, B. L., Aronov, A. G. & Spivak, B. Z. The Aharonov-Bohm effect in disordered conductors. *Pis'ma Zh. Eksp. Teor. Fiz.* **33,** 101–103 (1981); *JETP Lett.* **33,** 94–97 (1981).